

## Multimode Ion-Photon Entanglement over 101 Kilometers

V. Krutyanskiy<sup>1,2,\*</sup>, M. Canteri<sup>1,2</sup>, M. Meraner<sup>1</sup>, V. Krcmarsky<sup>2,1</sup> and B.P. Lanyon<sup>1,2</sup>

<sup>1</sup>*Institut für Experimentalphysik, Universität Innsbruck, Technikerstrasse 25, Innsbruck 6020, Austria*

<sup>2</sup>*Institut für Quantenoptik und Quanteninformation, Österreichische Akademie der Wissenschaften, Technikerstrasse 21a, Innsbruck 6020, Austria*

(Received 7 August 2023; revised 23 December 2023; accepted 5 March 2024; published 10 April 2024)

A three-qubit quantum network node based on trapped atomic ions is presented. The ability to establish entanglement between each individual qubit in the node and a separate photon that has traveled over a 101-km-long optical fiber is demonstrated. By sending those photons through the fiber in close succession, a remote entanglement rate is achieved that is greater than when using only a single qubit in the node. Once extended to more qubits, this multimode approach can be a useful technique to boost entanglement-distribution rates in future long-distance quantum networks of light and matter.

DOI: 10.1103/PRXQuantum.5.020308

### I. INTRODUCTION

Envisioned quantum networks consist of matter-based nodes for information processing and storage, which are interconnected with photonic links for the establishment of entanglement between the nodes [1,2]. Such networks could span distances from a few meters to a worldwide quantum network and would enable applications in computing, sensing, and communication. Photon-mediated entanglement has been established across elementary networks consisting of two [3–11] and three [12] remote matter qubits, distributed over distances up to 1.5 km [13]. Recently, two atoms 400 m apart have been entangled over a spooled 33 km-long fiber channel [14].

A key requirement for long-distance quantum networking is the ability to entangle a matter qubit with a photon and to distribute that photon over many tens of kilometers. That ability has been demonstrated using a range of different systems including trapped ions [15–17] and atoms [18], for distances of up to 50 km [17]. A second key requirement is the ability to integrate multiple quantum logic capable qubits into network nodes [2]. Nodes consisting of two cotrapped atoms [19], two qubits in a diamond-defect system [20], and two cotrapped ions [21–24] have been demonstrated.

One advantage of having multiple qubits in network nodes is the possibility of performing *multimode*

entanglement distribution [25,26]. With a single matter qubit, one has to wait for at least the light travel time to learn whether entanglement distribution was successful between nodes before trying again; otherwise, entanglement with the first photon is lost. For example, over 100 km of optical fiber, the light travel time limits the maximum attempt rate for establishing remote entanglement to 1 kHz, which, given the 1% transmission probability using standard optical fibers at 1550 nm, would yield a maximum possible success rate of 10 Hz. This limit could be overcome by sending many photons into the channel, each entangled with a different matter qubit in the node and thereby performing multiple entanglement-distribution attempts within the single-photon travel time.

Quantum memories capable of multimode photon storage have been proposed [25,27], demonstrated [28–31], and used to increase the rate of memory-photon entanglement over up to 5 km of optical fiber, limited by the memory storage time of a few tens of microseconds [32]. A key next step is to interface multimode quantum memories with qubit registers capable of quantum processing, as envisioned for the most advanced forms of a quantum network [2].

In this paper, we present two main results. First, entanglement between a matter qubit and a photonic qubit is achieved over a spooled 101-km-long fiber channel: twice the distance of previous works (see, e.g., Refs. [15–18]) and requiring a matter-qubit coherence time on the order of the photon travel time (494  $\mu$ s) to achieve. Second, using three cotrapped matter qubits in the node, we demonstrate a multimodelling enhancement for the rate of entanglement distribution. Our node is capable of universal deterministic quantum computing, as demonstrated for two ions in Ref. [23], and our approach offers a path to enhance the rate for

\*viktor.krutianskii@uibk.ac.at

Published by the American Physical Society under the terms of the [Creative Commons Attribution 4.0 International license](#). Further distribution of this work must maintain attribution to the author(s) and the published article's title, journal citation, and DOI.

entangling remote quantum processors over long distances, either directly or in combination with multimode quantum memories.

## II. EXPERIMENTAL SETUP AND SEQUENCE

A conceptual schematic of the experimental setup is presented in Fig. 1 and is now summarized. Our network node includes three  $^{40}\text{Ca}^+$  ions confined in a three-dimensional (3D) linear Paul trap and at the position of the waist of an optical cavity for photon collection at 854 nm [33,34]. The ions are positioned at antinodes of the vacuum-cavity standing wave. Because the cavity axis is not quite perpendicular to the ion-string axis (differing by a designed angle of  $5^\circ$ ), it is not possible to position the ions in the same antinode. Instead, there is a unique axial confinement (and a corresponding axial center-of-mass frequency,  $\omega_z$ ) at which the ions can be positioned in neighboring antinodes. A calibration process is performed to find that unique value (see Appendix A), yielding  $\omega_z = 0.869(20)$  MHz. Given  $\omega_z$ , we calculate that the ion spacing is  $5.26(10)$   $\mu\text{m}$  and that the angle between the ion string and the cavity axis is  $85.3(1)^\circ$ .

Single photons are generated via a bichromatic cavity-mediated Raman transition (BCMRT) [33,36], driven via a 393-nm Raman laser beam with a  $1.2\text{-}\mu\text{m}$  waist at the ions [23]. The advantages of the BCMRT over other schemes are discussed in e.g., Ref. [36]. A Raman laser pulse on an ion in the state  $|S\rangle = |4^2S_{1/2}, m_j = -1/2\rangle$  ideally generates the maximally entangled state

$$|\psi(\theta)\rangle = (|D', V\rangle + e^{i\theta}|D, H\rangle)/\sqrt{2}, \quad (1)$$

where  $|D'\rangle$  and  $|D\rangle$  are the respective Zeeman states  $|3^2D_{5/2}, m_j = -3/2\rangle$  and  $|3^2D_{5/2}, m_j = -5/2\rangle$ ,  $|V\rangle$  and  $|H\rangle$  are the respective vertical and horizontal polarization

components of a single photon emitted into the cavity vacuum mode, and  $\theta$  is a phase set by the relative phase of the two frequency components in the bichromatic beam [36]. After exiting the vacuum chamber through an optical view port, photons are coupled into single-mode optical fiber and then converted to 1550 nm (the telecom C band) via the polarization-preserving single-photon frequency-conversion system of Refs. [17,35]. Telecom photons are then sent into a 101-km-long single-mode fiber channel with a calculated photon travel time of 494  $\mu\text{s}$  and a measured total transmission probability of 1.36(4)%. The fiber channel consists of two 50.4-km spools, connected with a fiber joiner. The first (following the photon path) coil rests on an optical table and is covered by a plastic shielding provided by the manufacturer. The second coil is placed into an additional plastic box, providing thermal and room-light shielding, which rests on the same optical table. The spools are in a laboratory the average temperature of which is stabilized at the level of  $\pm 0.5^\circ\text{C}$ . Neither the optical length nor temperature of the fiber channel is actively stabilized. Nevertheless, the fidelity between output polarization states measured 1 h apart typically remains over 0.99. The polarization dynamics in an unspooled fiber [37] could be actively controlled using methods developed in the field of quantum cryptography (see, e.g., Ref. [38]). Finally, the photon polarization is analyzed in a chosen basis using a combination of motorized wave plates, a polarizing beam splitter, and two superconducting nanowire single-photon detectors (SNSPDs) [Fig. 1(d)].

The experimental pulse sequence consists of three parts: initialization, photon generation, and ion-qubit measurement. Initialization consists of 7 ms of Doppler cooling followed by 20  $\mu\text{s}$  of optical pumping into the state  $|S\rangle$ . Photon generation consists of a sequence of pulses that we call an attempt, which is repeated up to 15 times

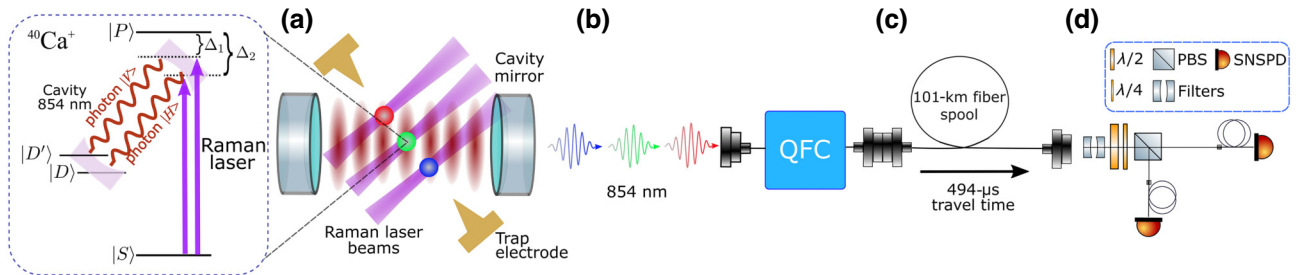


FIG. 1. The experimental schematic. (a) Three  $^{40}\text{Ca}^+$  ions at neighboring antinodes of an 854-nm vacuum standing-wave mode in an optical cavity. Sequential laser pulses, one on each ion, generate three photons, each entangled by polarization to the ion that emitted it. The inset shows the atomic energy-level diagram:  $|S\rangle = |4^2S_{1/2}, m_j = -1/2\rangle$ ,  $|P\rangle = |4^2P_{3/2}, m_j = -3/2\rangle$ ,  $|D\rangle = |3^2D_{5/2}, m_j = -5/2\rangle$ , and  $|D'\rangle = |3^2D_{5/2}, m_j = -3/2\rangle$ . The frequency difference  $\Delta_2 - \Delta_1$  is equal to that between  $|D'\rangle$  and  $|D\rangle$ . (b) The photons are converted to 1550 nm via quantum frequency conversion (QFC), using the system of Refs. [17,35]. (c) A 101-km-long single-mode spooled fiber channel (SMF-28). (d) Polarization analysis involving half ( $\lambda/2$ ) and quarter ( $\lambda/4$ ) wave plates, a filter network, a polarizing beam splitter (PBS), and superconducting nanowire single-photon detectors (SNSPDs). The narrowest element of the filter network is an air-spaced Fabry-Perot cavity with a 250-MHz line width, centered at 1550 nm [17].

(15 attempts). Each attempt begins with 50  $\mu\text{s}$  of Doppler cooling and 20  $\mu\text{s}$  of optical pumping, which serve to reinitialize the ions after any previous attempt. Next comes a 50- $\mu\text{s}$  Raman laser pulse on each ion sequentially, spaced by 12  $\mu\text{s}$  to allow, e.g., the laser focus to be switched between ions using an acousto-optic deflector. The ideal result is a train of three photons, in which each photon is maximally entangled with the ion that emitted it. Next comes a 503- $\mu\text{s}$  wait time to allow all three photons to traverse the 101 km fiber channel and be detected. At the beginning of that wait time, the  $|D\rangle$  electron population of all ions is moved to the state  $|S\rangle$  via an 6.4- $\mu\text{s}$   $\pi$  pulse, using a laser at 729 nm. As such, the ion qubits are encoded in superpositions of the  $|S\rangle$  and  $|D'\rangle$  states while the photons travel. After 243.6  $\mu\text{s}$  of the wait time from the last 729-nm pulse, a 729-nm  $\pi$  pulse then swaps the  $|S\rangle$  and  $|D'\rangle$  populations of all ion qubits, realizing a spin echo. The pulse sequence for a single attempt is now completed. In the cases in which no photons are detected within the expected arrival-time windows, another attempt is performed. In the cases in which at least one photon is detected within the expected arrival-time windows, further attempts are aborted and ion-qubit measurement is executed.

Ion-qubit measurement begins with an optional 729-nm  $\pi/2$  pulse implemented on the  $|S\rangle$  to  $|D'\rangle$  transition on all ions. The optional pulse is implemented when the ion qubits are to be measured in the Pauli  $\sigma_x$  or  $\sigma_y$  basis: we set the optical phase of the pulse to determine in which of the two bases the measurement is made. The optional pulse is not implemented when the ion qubit is to be measured in the  $\sigma_z$  basis. Finally, single-ion resolved-state detection is performed via electron shelving for 1.5 ms on all three ions simultaneously, at which point the experimental sequence is concluded. The chosen ion-qubit measurement basis and photon polarization-qubit measurement are fixed throughout a single execution of the experimental pulse sequence.

The experimental pulse sequence is repeated sufficiently many times, and in sufficiently many measurement bases, to allow for reconstruction of the two-qubit states  $\rho_{ij}$  of all nine possible combinations of one ion qubit ( $i$ ) and one photon qubit ( $j$ ), via state tomography. States are reconstructed via the maximum-likelihood method and are conditional on successful detection of photon  $j$ . Uncertainties in parameters derived from the states  $\rho_{ij}$  are obtained via the Monte Carlo technique. We use the concurrence  $C$  [39] to quantify the degree of entanglement in the states  $\rho_{ij}$ , where  $0 \leq C \leq 1$  and  $C = 1$  is a maximally entangled state achieved, e.g., by the state of Eq. (1).

### III. EXPERIMENTAL RESULTS

In our first experiment, we characterize the ion-photon states  $\rho_{ij}$  before the photon-conversion setup, at the

emitted photon wavelength of 854 nm. For those states, we use the new notation  $\rho_{ij}^0$ , reflecting that the photons have traveled over 0 km of fiber. A modified setup is used in which the fiber-coupled photons after the cavity output are sent to a polarization-analysis setup that is similar to the one shown in Fig. 1 but with optics and detectors optimized for 854 nm. The experimental pulse sequence has the following differences compared to the one described in the previous section: only one attempt to make a photon train is made per sequence, the 503  $\mu\text{s}$  wait time is removed as well as the spin echo, and a Raman pulse length of 60  $\mu\text{s}$  is used on each ion.

The modified pulse sequence was implemented over a 42-min period, during which  $A = 41\,645$  attempts were made to generate a photon from each ion. In Fig. 2(a), we show a histogram of the single-photon detection events, in which three single-photon wave packets are clearly visible. The photons detected in the first, second, and third 65- $\mu\text{s}$ -long time windows are the ones expected to have been produced due to the corresponding Raman laser pulse applied to the first, second, and third ion, respectively. The total number of counts recorded in those windows are 13 127, 14 465, and 13 326, corresponding to estimated detection probabilities for 854-nm photons of 0.315(3), 0.347(3), and 0.320(3), where the uncertainties are based on Poissonian photon detection statistics. As discussed later, the middle ion is expected to yield photons with the highest probability, since that ion is positioned in the middle of the cavity waist (Appendix A), where the ion-cavity coupling strength is highest. Only in 14 attempts has more than one detection event been registered in the same time window, illustrating the single-photon character of our source. In  $N_{\text{single}} = 18\,337$  cases, exactly one photon detection event was registered in one of the windows. In  $N_{\text{double}} = 9037$  cases, exactly two photon detection events were registered in different windows. In  $N_{\text{triple}} = 1485$  cases, exactly three detection events were registered in different windows. The total probability of detecting at least one photon within one photon generation attempt was  $(N_{\text{single}} + N_{\text{double}} + N_{\text{triple}})/A = 0.693(4)$ . The expectation value of the number of photons detected in an attempt was  $(N_{\text{single}} + 2 \times N_{\text{double}} + 3 \times N_{\text{triple}})/A = 0.981(5)$ .

Each measured single-photon wave packet in Fig. 2(a) is well described by a theoretical model based on a master equation, with model parameters for each wave packet that differ only in the values used for the ion-cavity coupling strengths of the corresponding ion (see Appendix B). The differences in those values are consistent with the effect of the Gaussian profile of the vacuum-cavity mode across the ion string. The simulations include an overall detection-path efficiency of 0.518 for each of the photons, which is consistent with a value of 0.53(3) obtained from independent calibrations (see Appendix C). The detection-path efficiency includes all losses encountered by a photon after emission into the cavity, including the finite probability

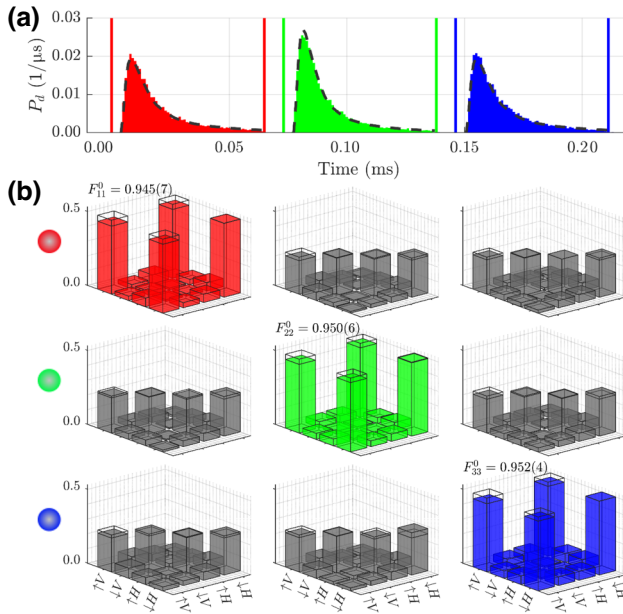


FIG. 2. Ion-photon entanglement over 0 km. (a) Histograms of 854-nm photon arrival times. Probability densities are shown on the vertical axis: the number of counts normalized by the number of attempts  $A$  and by the time-bin width of 1  $\mu\text{s}$ , measured before QFC in Fig. 1 and without the fiber channel. Three single-photon wave packets are visible. Color is used to demarcate the ion that is expected to have produced the photon, following the ion-coloring scheme in Fig. 1. Time zero is when an acousto-optic modulator received a radio-frequency signal to send a laser pulse to ion 1. The detection efficiencies and quantum states are determined within the 65- $\mu\text{s}$ -long time windows shown via the colored vertical lines. The dashed black lines show the results of a theoretical model. (b) Absolute values of the measured density matrices  $\rho_{ij}^0$  of all nine ion-photon pairs. The ion (photon) involved in each row (column) is constant and is indicated by the colored ball on the left (photon wave packet above). States  $\rho_{i=j}^0$  are colored red, green, and blue. States  $\rho_{i \neq j}^0$  are shown in gray. The fidelities  $F_{i=j}^0$  of the states  $\rho_{i=j}^0$  with the state  $|\psi(0)\rangle\langle\psi(0)|$  (wire mesh) are labeled. For  $i \neq j$ , the wire mesh shows the fully depolarized states.

of exiting the cavity into the output mode (independently measured to be 0.78(2) [33]) all the way to the average 854-nm detector efficiencies (independently measured to be 0.87(2) [33]). The simulations predict probabilities of 0.575, 0.664, and 0.575 for emission of photons into the cavity from ions 1, 2, and 3, respectively. Lower detected photon efficiencies are achieved in this work, compared to Ref. [33], largely due to the lack of ground-state cooling and a suboptimal Raman-laser-beam direction with respect to the principal magnetic field (quantization) axis. Both issues could be corrected by reconfiguring the experimental setup in future.

In all of the density matrices presented in this paper, we use the following notion for ion-qubit states:  $|D'\rangle = |\uparrow\rangle$  and  $|S\rangle = |\downarrow\rangle$ . In Fig. 2(b), we present the absolute values

of all nine tomographically reconstructed two-qubit ion-photon density matrices  $\rho_{ij}^0$ . The concurrences of the three states,  $\rho_{11}^0$ ,  $\rho_{22}^0$ , and  $\rho_{33}^0$  are 0.90(1), 0.91(1), and 0.92(1), respectively, proving strongly entangled states. The concurrences of the remaining six states  $\rho_{i \neq j}^0$  are zero. The fidelities of the absolute values of the states  $\rho_{11}^0$ ,  $\rho_{22}^0$ , and  $\rho_{33}^0$ , with  $|\psi(0)\rangle$  (Eq. (1) for  $\theta = 0$ ) are  $F_{11}^0 = 0.945(6)$ ,  $F_{22}^0 = 0.950(5)$ , and  $F_{33}^0 = 0.952(4)$ , respectively. The fidelities of all the states  $\rho_{i \neq j}^0$  with the maximally mixed two-qubit state are greater than 0.96 to within three standard deviations of uncertainty. We use the fidelity defined as  $\text{Tr}(\rho_{i=j}^0 |\psi(0)\rangle\langle\psi(0)|)$ .

The entangled states  $\rho_{i=j}^0$  are locally rotated with respect to each other. Specifically, the phases of the large coherence terms ( $|\downarrow, H\rangle\langle\uparrow, V|$  and its complex conjugate) are  $0.731(5)\pi$ ,  $0.632(5)\pi$ , and  $0.530(7)\pi$ , for  $\rho_{11}^0$ ,  $\rho_{22}^0$ , and  $\rho_{33}^0$ , respectively. Those phases are consistent with a  $\sigma_z$  rotation of the ion-qubit states as a function of time due to an incorrect setting of the frequency difference between the two fields in the Raman laser drive by 689 Hz. That frequency difference should ideally be equal to the one between the  $|D\rangle$  and  $|D'\rangle$  states [Fig. 1(a)]. The incorrect setting was due to a miscalibration in the transition frequencies and could be reduced to below the hertz level by a more careful calibration using 729-nm spectroscopy. Alternatively, such frequency offsets can be corrected by spin echoes implemented on the ion qubits during the photon travel time, as we demonstrate in the next experiment. Imperfections in state initialization (optical pumping) and ion-qubit measurement (qubit rotation and electron shelving) are each expected to contribute less than 0.01 infidelity to the states  $\rho_{i=j}^0$ . The physical origins of the remaining imperfections in those states, and their relative contributions, are not yet known and identifying them will be the subject of future work. We conclude from analysis of the data in Fig. 2 that an 854-nm photon can be generated that is strongly entangled with any desired ion in the string.

In our second experiment, the ion-photon states  $\rho_{ij}$  are characterized using the full setup of Fig. 1. For these states, we use the new notation  $\rho_{ij}^{101}$ , reflecting that the photons have traveled over 101 km of optical fiber. Measurements were taken over 45 min, during which  $A^{101} = 882\,982$  attempts were made. In Fig. 3(a), we show a histogram of the recorded single-photon detection events. The three-photon wave packets are spaced over a total of 172  $\mu\text{s}$  and thus simultaneously fit well within the travel time of the fiber channel. The total number of counts recorded in the three sequential 50- $\mu\text{s}$ -long time windows were 572, 693, and 643, corresponding to detection probabilities of  $p_1 = 6.5(3) \times 10^{-4}$ ,  $p_2 = 7.8(3) \times 10^{-4}$ , and  $p_3 = 7.3(3) \times 10^{-4}$ , respectively. Only in two attempts was more than one detection event registered in the same time window. In  $N_{\text{single}} = 1900$  cases, exactly one photon

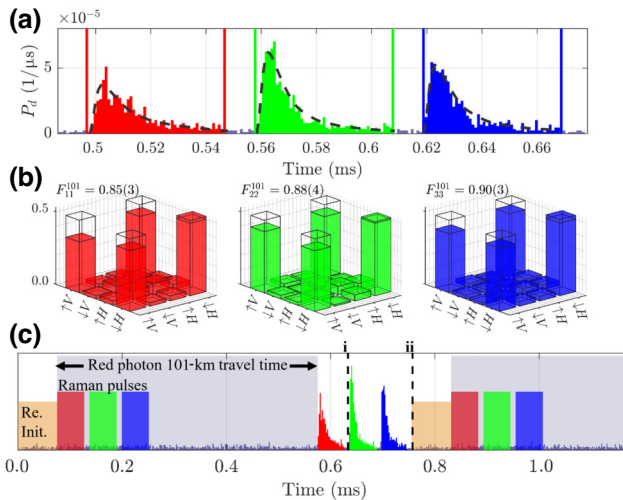


FIG. 3. Ion-photon entanglement over 101 km. (a) Histograms of 1550-nm-photon arrival times. Probability densities are shown on the vertical axis: normalized by the number of attempts  $A^{101}$  and by the time-bin width of 1  $\mu\text{s}$ , measured using the setup of Fig. 1. The color scheme is as described in Fig. 2. The dashed black lines show the results of a theoretical model. (b) The absolute values of the measured ion-photon density matrices  $\rho_{i=j}^{101}$ . The presented states are locally rotated from those reconstructed directly from the data, as described in the text. The fidelities  $F_{i=j}^{101}$  of the states  $\rho_{i=j}^{101}$  with the state  $|\psi(0)\rangle\langle\psi(0)|$  (wire mesh) are labeled. (c) The conceptual schematic of the experimental sequence. One attempt—Involving three Raman laser pulses—took 757  $\mu\text{s}$  (dashed line labeled “ii”). Attempts using a single ion would have taken 633  $\mu\text{s}$  (dashed line labeled “i”). “Re. Init.” is the 70- $\mu\text{s}$ -long cooling and optical pumping performed after each attempt.

detection event was registered in one of the windows. In  $N_{double} = 4$  cases, exactly two photon detection events were registered in different windows. There were no cases in which exactly three or more detection events were registered in different windows. The total probability of detecting (successfully distributing) at least one photon over 101 km per attempt was  $2.16(5) \times 10^{-3}$ . The expectation value of the number of photons detected in an attempt was also  $2.16(5) \times 10^{-3}$ .

The measured wave packets of Fig. 3(a) are well described by those from the master-equation model. The only model parameter values that differ from those used to produce the simulations in Fig. 2(a) are the following: a lower total detection-path efficiency of  $1.26 \times 10^{-3}$ ; the shorter Raman laser pulse used; a 7% lower Raman laser Rabi frequency; and ion-cavity coupling strengths that differ by up to 10%, consistent with an ion-string displacement by 1.4  $\mu\text{m}$  away from the cavity axis (see Appendix B). The lower path efficiency and Rabi frequencies are consistent with independent calibrations. The aforementioned displacement of the string away from the cavity waist was not independently verified. However, step

1 of the calibration process (Appendix A), which minimizes such displacements, had not been performed for a month before the data in Fig. 3 were taken and therefore a displacement of 1.4  $\mu\text{m}$  due to thermal effects is not unreasonable. There was a 3-week gap between taking the data in Fig. 2 and the data in Fig. 3.

In Fig. 3(b), we present the absolute values of the three tomographically reconstructed states  $\rho_{i=j}^{101}$ , after the same local two-qubit rotation was applied to each state. A local two-qubit rotation is a tensor product of single-qubit rotations—one to the ion and one to the photon—which cannot change the entanglement content. The method used to obtain that local rotation is now described. First, the data from all matched ion-photon pairs ( $i = j$ ) were added up and used to tomographically reconstructed a single ion-photon state  $\rho^{101}$ . Second, a numerical search was performed over local rotations that maximizes the fidelity of  $\rho^{101}$  with the state  $|\psi(0)\rangle\langle\psi(0)|$ , yielding the optimum local rotation and a fidelity of 0.89(2). The concurrence of the state  $\rho^{101}$  is 0.76(4). The concurrences of the states  $\rho_{11}^{101}$ ,  $\rho_{22}^{101}$  and  $\rho_{33}^{101}$  are 0.71(8), 0.80(6), and 0.83(6), respectively. After the local rotation, the fidelities of those states with  $|\psi(0)\rangle\langle\psi(0)|$  are  $F_{11}^{101} = 0.85(4)$ ,  $F_{22}^{101} = 0.88(3)$ , and  $F_{33}^{101} = 0.90(3)$ , respectively. No statistically significant rotation of the ion-qubit states with respect to each other is evident.

The results of the model described in Appendix D show that the infidelities in the tomographically reconstructed states  $\rho_{i=j}^{101}$  are statistically consistent with the effect of background telecom photon-detector counts alone, which occur at a rate of  $2.0(1) \text{ s}^{-1}$ . When the imperfections in the states  $\rho_{i=j}^0$  are included in that model, the predicted infidelities remain statistically consistent with the experimentally observed ones. The infidelities in the initial states  $\rho_{i=j}^0$  are of a similar size to the statistical uncertainties in the fidelities of the states  $\rho_{i=j}^{101}$  and therefore are not clearly resolved in the states  $\rho_{i=j}^{101}$ . Decoherence of the ion qubits during the 494- $\mu\text{s}$  photon travel time is insignificant: coherence times of 62(3) ms are expected in our system when using optical spin echoes [23] (for more details, see Appendix E).

We now turn to consider the achieved multimode enhancement. Each attempt in the 101-km experiment took  $\tau = 757 \mu\text{s}$  [Fig. 3(c)] and provided three opportunities to succeed in detecting a photon (one from each ion). The total probability for at least one successful photon detection per attempt was  $P = 2.16(5) \times 10^{-3}$ , which yields an effective success rate of  $P/\tau = 2.85(7) \text{ Hz}$ . If, instead, we had used only one ion in the string, completion of each attempt would have taken 633  $\mu\text{s}$  [Fig. 3(c)], as in addition to the reinitialization and photon generation times, one has to wait 494  $\mu\text{s}$  for the photon to travel and be detected before trying again. For the probability of success for that attempt, we take the value from our experiment,

for the most efficient central ion, of  $p_2 = 7.8(3) \times 10^{-4}$ . One then calculates a predicted effective success rate of 1.23(5) Hz for the single-ion case. Therefore, by using all three ions, we achieved an increase in the success rate by a factor of 2.3(1). That factor is reduced from the ideal value of 3 due to three separate effects: slightly lower photon-emission probabilities from the ions not in the center of the string; the times for switching the focus of the laser between the ions; and that we wait for all three photons to (potentially) arrive before trying to generate new photons. The last effect could be eliminated in future, after development of a single-ion-focused reinitialization scheme. Even considering a scenario in which the time for generating and reinitializing photons was effectively zero, such that each attempt took 494  $\mu$ s, the 101 km success rate for a single ion emitting in the string would still be only 1.59(7) Hz.

#### IV. CONCLUSIONS AND OUTLOOK

In conclusion, ion-photon entanglement was achieved over a 101-km-long fiber channel with a Bell-state fidelity largely limited by detector background counts. The use of three cotrapped ion qubits allowed entanglement to be distributed at a higher rate than when using a single ion, by overcoming the attempt-rate limit set by the photon travel time over the channel. In future, photon detection after the fiber channel could be used to swap entanglement to a duplicate remote ion-node via entanglement swapping [3,10,11]. Here, each remote node sends a photon train and coincident photon detection between different temporal pairs heralds entanglement of known remote ion pairs. The quantum processing and coherence times possible in ion-qubit registers could then be used to store the established entanglement for extended periods of time, as well as to purify the distributed entanglement and to increase the number of remote Bell pairs over time.

The multimoding depth in our system could be significantly increased in future by coupling more ions in the node to traveling photons. For example, longer ion strings could perhaps be shuttled stepwise through the cavity mode by modulating the trap electrode voltages, allowing generation of a photon from each one. Alternatively, a single stationary ion could be used to generate photons sequentially and have its quantum state transferred to cotrapped ions after each attempt via quantum logic operations, as demonstrated for two ions in Ref. [24]. Benefiting from multimoding with hundreds or thousands of ions would require significant shortening of the current single-photon wave-packet lengths [Fig. 3(a)] such that they all fit simultaneously within the light travel time. Achieving that without compromising photon generation efficiency requires an increased ion-cavity coupling strength afforded, e.g., by smaller-mode-volume cavities [40–42].

Our data sets are available online [43]

*Note added.*—We recently became aware of the related work by Zhou *et al.* [44].

#### ACKNOWLEDGMENTS

This research was funded in part by the Austrian Science Fund (FWF) [Grant DOIs: 105576/Y849, 105576/P34066 and 105576/F7116]. We acknowledge support from the Österreichische Nationalstiftung für Forschung, Technologie und Entwicklung (AQUnet project). This work has also received funding from the DIGITAL-2021-QCI-01 Digital European Program under Project No. 101091642 and project name “QCI-CAT,” and the European Union’s Horizon Europe research and innovation program under Grant Agreement No. 101102140 and project name “QIA-Phase 1.” We acknowledge funding for V.Kru. by the Erwin Schrödinger Center for Quantum Science & Technology (ESQ) Discovery Programme, and for B.P.L. by the CIFAR Quantum Information Science Program of Canada. The opinions expressed in this document reflect only the authors’ views and reflect in no way those of the European Commission. The European Commission is not responsible for any use that may be made of the information that it contains. V.Kru., M.M., V.Krc., and M.C. took the experimental data. V.Kru., M.C., M.M., and B.P.L. developed the experimental setup. V.Kru., M.C., M.M., and B.P.L. carried out the data analysis and interpretation. The modeling was done by V.Kru. The manuscript was written by B.P.L. and V. Kru. and all authors provided detailed comments. The project was conceived and supervised by B.P.L.

#### APPENDIX A: POSITIONING THE ION STRING IN THE CAVITY

The process is carried out in three steps. The goal of the first step is to overlap the center of the ion trap (equivalently, the middle ion in the string) with the center of the waist of the 854-nm TEM<sub>00</sub> mode of the cavity. This is achieved using a single ion following the method described in Ref. [33, Appendix B. 1d].

The goal of the second step is to obtain an ion-ion distance such that, when projected onto the cavity axis, the ions are spaced by 427 nm: the distance between nodes (and antinodes) in the 854-nm vacuum-cavity standing wave. That is achieved by varying the axial confinement of the three-ion string and, for each value, performing measurements similar to those presented and explained in Ref. [45]. Specifically, we record the 854-nm photons when illuminating all three ions with a broadly focused 393-nm beam together with an 854-nm and 866-nm repumper. For each axial confinement, we minimize the rate of the detected 854-nm cavity photons by fine adjustment of the cavity position along its axis using an in-vacuum translation stage. The axial confinement that offers the lowest count rate is found and interpreted as the situation in which

each ion is located at a node of the vacuum-cavity standing wave.

The goal of the third step is to position each of the three ions at a cavity antinode. That is achieved using the single-ion focused Raman beam and repumpers to generate cavity photons from the central ion, then adjusting the cavity position along its axis using in-vacuum translation stages until the count rate is maximized.

An angle of  $5^\circ$  off perpendicular, between the ion string and cavity axes, was chosen in the design of the ion-trap system. With that angle, and with practical ion string confinement strengths, it is possible to position either two ions simultaneously into cavity maxima, or one ion in a cavity maximum and the other in a cavity minimum. In principle, the latter configuration offers another way to generate a photon from an individual ion in a string.

## APPENDIX B: NUMERICAL SIMULATIONS OF PHOTON WAVE PACKETS

The numerical simulations were performed to obtain an estimation for the photon generation efficiencies and single-photon wave packets. Specifically, the master-equation model of the laser-atom-cavity system is used from Ref. [33]. The model parameters include the experimental geometries of the Raman laser, cavity, and magnetic field, which are the same as described in Ref. [23] (in particular, see Secs. I.B and III.C of the Supplemental Material in the cited reference).

A key model parameter is the maximum strength of the coherent coupling between a single photon in the cavity and a single ion, which is calculated to be  $g_0 = 2\pi \times 1.53$  MHz in our system, based on the cavity geometry and the properties of the atomic transition. Here, we consider the  $|P\rangle - |D\rangle$  and  $|P\rangle - |D'\rangle$  transitions but do not take into account the different Clebsch-Gordon coefficients for the two transitions or the projection of the transition polarizations onto the cavity-photon polarizations, both of which are accounted for separately in the simulations [36]. The coupling strength of the bichromatic cavity-mediated Raman transition on a given ion in a string is reduced by, e.g., the motion of the ion in the trap and by any displacement of the position of the ion away from the cavity axis. We model those effects using a reduced ion-cavity coupling strength for ion  $i$  as  $g_i = x_i \gamma g_0$ , where  $0 \leq x_i \leq 1$  and  $0 \leq \gamma \leq 1$ . The parameter  $x_i$  quantifies any reduction in ion-cavity coupling strength due to ion  $i$  not being positioned at the cavity axis. The parameter  $\gamma$  quantifies any other reduction in the coupling strength of the bichromatic cavity-mediated Raman process e.g., due to the motion of the ion in the trap. We use a single value for  $\gamma$  for all ions and determine its value by comparing measured single-photon temporal wave packets with simulated wave packets based on numerical integration of the master equation for a range of values of the coupling strength [33].

Another key model parameter is the strength of the bichromatic drive. In order to determine that strength, we measure the ac Stark shift of the Raman transition via spectroscopy, as described in Secs. I.B and III.C of the Supplemental Material of Ref. [23]. The bichromatic drive field polarization in the experiment (and the simulations) is set to linear and perpendicular to the magnetic field and thus consists of an equal superposition of two circularly polarized components,  $\sigma^-$  and  $\sigma^+$ . While only the  $\sigma^-$  component is set to resonantly drive the bichromatic cavity-mediated Raman transition, both polarization components contribute to the ac Stark shift. In the simulations, we set the strength of the bichromatic drive  $\Omega^-$ —the Rabi frequency with which the  $\sigma^-$  transition  $|S\rangle = |4^2S_{1/2}, m_j = -1/2\rangle$  to  $|4^2P_{3/2}, m_j = -3/2\rangle$  is driven—to the value for which the model predicts the same total ac Stark shift as measured in the experiment. The model requires specifying both Rabi frequencies,  $\Omega_1^-$  and  $\Omega_2^-$ , of the two  $\sigma^-$ -polarized frequency components of the bichromatic drive. Here,  $\Omega_1^-$  denotes the component that drives  $|S\rangle - |D'\rangle$  and results in a vertically polarized ( $V$ ) photon and  $\Omega_2^-$  denotes the component that drives  $|S\rangle - |D\rangle$  and results in a horizontally polarized ( $H$ ) photon. For all the simulations, we set  $(\Omega_1^-)^2 + (\Omega_2^-)^2 = (\Omega^-)^2$  and  $\Omega_1^- / \Omega_2^- = 0.81$ —the values for which the model predicts equal probabilities for the generation of the  $H$ - and  $V$ -polarized photons.

We now provide more information about the simulations for the experiment in which 854-nm photons are detected, shown in Fig. 2. By considering the ion string to be centered around the cavity axis and, from the Gaussian cavity-mode profile, we calculate the values of  $\{x_i\}$  to be 0.83, 1, and 0.83 for the three ions. Next,  $\gamma = 0.784$  is found to provide a close match between the measured and simulated wave packets. We measured an ac Stark shift of the Raman transition of 0.88(2) MHz for all the three ions. In the simulations, we use the value of  $\Omega^- = 2\pi \times 31.47$  MHz, for which the model predicts an ac Stark shift of the Raman transition of 0.88 MHz.

We now provide more information about the simulations for the experiment in which 1550-nm photons are detected, shown in Fig. 3. We use  $\gamma = 0.784$ , as found using the data of Fig. 2. We use  $\{x_i\}$  values of 0.739, 0.987, and 0.894, which are calculated from the Gaussian cavity-mode profile in the case of a 1.4- $\mu\text{m}$  displacement of the ion string along the trap-axis direction with respect to the center of the cavity mode. This shift is found by comparing simulated wave packets and another experiment performed on the same date as the one presented in Fig. 3 but involving 50 km of fiber instead of 101 km (in which the measurement statistics are better due to the higher photon detection efficiency). In the 101-km experiment, we measured ac Stark shifts of the Raman transition of 0.82(2) MHz for all the three ions. In the simulations, we used the value of

$\Omega^- = 2\pi \times 30.41$  MHz, for which the model predicts ac Stark shifts of the Raman transition of 0.82 MHz.

## APPENDIX C: PHOTON PATH EFFICIENCY

Here, a detailed efficiency budget is presented for the photon detection path. When not given explicitly, uncertainties in given probabilities are half of the last significant digit. The beginning of each element in the following list gives the probability associated with a distinct part or process in the experiment. The detection-path efficiencies provided in the main text should be compared with a product of these probabilities (or a subset thereof, for the data taken involving 854-nm photons). For the photons detected at 854 nm, the total probability of the list is 0.53(3). For the photons detected at 1550 nm, the total probability of the following list is  $15(1.2)10^{-4}$ :

- (1) 0.78(2): the probability that, once a cavity photon is emitted into the cavity, the photon exits the cavity into free space on the other side of the output mirror [33].
- (2) 0.96(1): the transmission of free-space optical elements that are between the cavity output mirror and first fiber coupler (see  $P_{el}$  in Ref. [33]).
- (3) 0.81(3): the efficiency of coupling the photons into the first single-mode fiber [33]. Rather, this value should be considered an upper bound, since it was measured some days before the data presented in this paper were taken. We anticipate that coupling could be improved in future with better couplers and an antireflection-coated fiber end facet.
- (4) In the event of detection of 854-nm photons (Fig. 2), the lists ends here with 0.87(2): the detection efficiency of either of the single-photon detectors for 854 nm [33]. In the event of detection of 1550-nm photons (Fig. 3), this item is not relevant and the list continues.
- (5) 0.30(1): the photon transmission and conversion probability starting from the input fiber of the QFC setup [Fig. 1(b)] and up to the PBS shown in Fig. 1(d). This value is measured by replacing the 101-km fiber with a 1-m-long fiber.
- (6) 0.0136(4): the measured transmissions of the 101-km fiber, consisting of two 50.4-km SMF-28 fiber spools and one fiber connector. For the position of the fiber in the optical path, see Fig. 1(c).
- (7) 0.95: the transmission of a fiber joiner present in the path.
- (8) 0.83(3): the efficiencies of coupling the telecom photons into the single-mode fibers of the detector [see Fig. 1(d)].
- (9) 0.75(2): the detection efficiency of either of the telecom single-photon detectors [23].

For the experiment over 101 km of fiber, the Raman pulse (50  $\mu$ s long) was terminated when the photon detection probability became comparable with the background count probability [see Fig. 3(a)]. For the experiment at 854 nm over 0-km of fiber, a 60- $\mu$ s-long Raman pulse was used. Consideration of only photons detected within the first 50  $\mu$ s of the recorded wave packet during the 854-nm experiment reduces the photon detection efficiency by a factor of only 0.985.

## APPENDIX D: INFIDELITY DUE TO PHOTON-DETECTOR BACKGROUND COUNTS

We model the effect of background photon-detector counts on the 1550-nm ion-photon states  $\rho_{i=j}^{101}$  presented in Fig. 3 (defined as a detector click that did not result from a photon from the ion). For this, the background count rate is extracted from the measured counts in the tomography experiments by looking far outside the time windows in which the photons from the ions arrive and summing the contributions from both detectors, giving  $2.0(1)$   $s^{-1}$ . The origins of the background counts are independently estimated to be the following:  $1.2(2)$   $s^{-1}$  combined dark counts of two single-photon detectors as specified by the manufacturer; and a  $0.6(2)$   $s^{-1}$  count rate from the QFC setup photon noise after traversing 101 km of fiber. The infidelity that the measured  $2.0(1)$   $s^{-1}$  background counts would contribute, when added to some input state  $\rho^{input}$ , is simulated numerically. Specifically, first, the measurement-outcome probabilities expected for the state  $\rho^{input}$  are calculated. Second, for each ion  $i$ , these probabilities are renormalized such that their sum in each basis equals  $p'_i$ , the background-subtracted probability to detect a photon that belongs to the state  $\rho_{ii}^{101}$  when averaged over all measurement bases. Third, the average probability of a background count occurring in the corresponding window per measurement outcome is added to the probabilities obtained at the previous step. Fourth, new “noisy” state density matrices are reconstructed via maximum-likelihood tomography from the result of the previous step. Finally, the maximum observable fidelities are calculated from those “noisy” density matrices. When using the ideal Bell state ( $\rho^{input} = |\psi(0)\rangle\langle\psi(0)|$ ) as the input and the background count rate of  $2$   $s^{-1}$ , we calculate the maximum observable fidelities to be 0.88, 0.90, and 0.90 for the three ion-photon pairs, respectively, as ordered elsewhere in the paper. Separately, when using the experimentally reconstructed states  $\rho_{i=j}^0$  as the input and the same background count rate, we calculate the maximum observable fidelities to be 0.84, 0.87, and 0.86. All of these fidelities are all statistically consistent with the ones obtained in the experiment, of 0.85(4), 0.88(3), and 0.90(3).

The effect of the background photon-detector counts on the 854-nm ion-photon states  $\rho_{i=j}^0$  is calculated analogously and found to be smaller than the statistical uncertainty in the reconstruction of those states. At 854 nm, the measured background count rate was  $20.9(1) \text{ s}^{-1}$ : an order of magnitude higher than at 1550 nm. However, the higher background rate is more than compensated by the significantly increased photon detection probabilities at 854 nm, which are more than 2 orders of magnitude higher than those at 1550 nm.

## APPENDIX E: ION-QUBIT COHERENCE TIME

During the 494- $\mu\text{s}$  photon travel time over the 101-km fiber, the ion qubit is encoded in the  $|S\rangle = |4^2S_{1/2}, m_j = -1/2\rangle$  and  $|D'\rangle = |3^2D_{5/2}, m_j = -3/2\rangle$  states. We study the coherence of that qubit in the absence of the spin-echo pulse by performing a series of Ramsey-type experiments. From these experiments, we identify two major sources of noise that motivate the use of the spin echo. First, we observe changes of the static magnetic field on a time-scale of several minutes due to changes of the position of a nearby elevator. Those changes result in a shift of up to 250 Hz of the aforementioned transition. We calculate that such a shift, when randomly occurring in half of the experimental realizations of a Ramsey experiment, would result in the Ramsey-contrast decrease by 2% after 500  $\mu\text{s}$ .

In Fig. 4, we present the results of the Ramsey experiments when the elevator position is fixed, and without spin echoes, for up to a 10-ms waiting time. Additional experiments reveal that the coherence is limited by noise at 50 Hz, resulting in nonmonotonous coherence dynamics

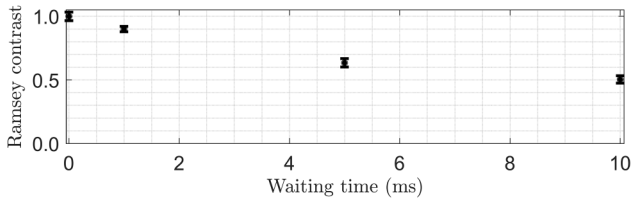


FIG. 4. The decoherence of the ion qubit in the absence of spin echoes. The qubit is encoded into the states  $|S\rangle$  to  $|D'\rangle$ . The Ramsey contrast is measured as a function of the waiting time. No spin-echo pulses are executed and the position of a nearby magnetic elevator is fixed. For each value of the waiting time, the following experiment is performed: After a single ion is initialized in the  $|S\rangle$  state, two laser-driven  $\pi/2$  pulses are performed on the qubit transition, separated by the waiting time. By scanning the optical phase  $\phi$  of the second  $\pi/2$  pulse, and measuring the excitation probability  $P_e$  of the ion, standard Ramsey oscillations are obtained. The Ramsey contrast of the oscillation  $C$  is obtained as a fit parameter using the fitting function  $P_e = y_0 + C \sin(\phi - \phi_0)/2$ . The error bars represent the statistical uncertainty of the fit.

beyond 10 ms. Specifically, we separately perform Ramsey experiments synchronized with the 50-Hz power-line cycle and measure the variation of the qubit transition frequency of up to 80 Hz in the cycle.

As both of the mentioned noise sources fluctuate over time scales that are long compared to the 494- $\mu\text{s}$  photon travel time, they are expected to be suppressed by the spin-echo  $\pi$  pulse used in the middle of the photon travel time, described in Sec. II. The infidelity introduced by that  $\pi$  pulse is measured to be below 1%. For more details on the limits of the coherence of our network node, including more complex spin-echo sequences that yielded coherence times exceeding 100 ms, see Sec. III.B.4 in the Supplemental Material of Ref. [23].

- [1] H. J. Kimble, The quantum Internet, *Nature* **453**, 1023 (2008).
- [2] S. Wehner, D. Elkouss, and R. Hanson, Quantum Internet: A vision for the road ahead, *Science* **362** (2018).
- [3] D. L. Moehring, P. Maunz, S. Olmschenk, K. C. Younge, D. N. Matsukevich, L.-M. Duan, and C. Monroe, Entanglement of single-atom quantum bits at a distance, *Nature* **449**, 68 (2007).
- [4] S. Ritter, C. Nölleke, C. Hahn, A. Reiserer, A. Neuzner, M. Uphoff, M. Mücke, E. Figueroa, J. Bochmann, and G. Rempe, An elementary quantum network of single atoms in optical cavities, *Nature* **484**, 195 (2012).
- [5] J. Hofmann, M. Krug, N. Ortegel, L. Gérard, M. Weber, W. Rosenfeld, and H. Weinfurter, Heralded entanglement between widely separated atoms, *Science* **337**, 72 (2012).
- [6] H. Bernien, B. Hensen, W. Pfaff, G. Koolstra, M. Blok, L. Robledo, T. Taminiau, M. Markham, D. Twitchen, L. Childress, and R. Hanson, Heralded entanglement between solid-state qubits separated by three metres, *Nature* **497**, 86 (2013).
- [7] A. Delteil, Z. Sun, W.-b. Gao, E. Togan, S. Faelt, and A. Imamoglu, Generation of heralded entanglement between distant hole spins, *Nat. Phys.* **12**, 218 (2016).
- [8] R. Stockill, M. J. Stanley, L. Huthmacher, E. Clarke, M. Hugues, A. J. Miller, C. Matthiesen, C. Le Gall, and M. Atatüre, Phase-tuned entangled state generation between distant spin qubits, *Phys. Rev. Lett.* **119**, 010503 (2017).
- [9] P. Magnard, S. Storz, P. Kurpiers, J. Schär, F. Marxer, J. Lütolf, T. Walter, J.-C. Besse, M. Gabureac, K. Reuer, A. Akin, B. Royer, A. Blais, and A. Wallraff, Microwave quantum link between superconducting circuits housed in spatially separated cryogenic systems, *Phys. Rev. Lett.* **125**, 260502 (2020).
- [10] L. J. Stephenson, D. P. Nadlinger, B. C. Nichol, S. An, P. Drmota, T. G. Ballance, K. Thirumalai, J. F. Goodwin, D. M. Lucas, and C. J. Ballance, High-rate, high-fidelity entanglement of qubits across an elementary quantum network, *Phys. Rev. Lett.* **124**, 110501 (2020).
- [11] V. Krutyanskiy, M. Galli, V. Kremarsky, S. Baier, D. A. Fioretto, Y. Pu, A. Mazloom, P. Sekatski, M. Canteri, M. Teller, J. Schupp, J. Bate, M. Meraner, N. Sangouard, B.

- P. Lanyon, and T. E. Northup, Entanglement of trapped-ion qubits separated by 230 meters, *Phys. Rev. Lett.* **130**, 050803 (2023).
- [12] M. Pompili, S. L. N. Hermans, S. Baier, H. K. C. Beukers, P. C. Humphreys, R. N. Schouten, R. F. L. Vermeulen, M. J. Tiggelman, L. dos Santos Martins, B. Dirkse, S. Wehner, and R. Hanson, Realization of a multinode quantum network of remote solid-state qubits, *Science* **372**, 259 (2021).
- [13] B. Hensen, H. Bernien, A. E. Dréau, A. Reiserer, N. Kalb, M. S. Blok, J. Ruitenberg, R. F. L. Vermeulen, R. N. Schouten, C. Abellán, W. Amaya, V. Pruneri, M. W. Mitchell, M. Markham, D. J. Twitchen, D. Elkouss, S. Wehner, T. H. Taminiau, and R. Hanson, Loophole-free Bell inequality violation using electron spins separated by 1.3 kilometres, *Nature* **526**, 682 (2015).
- [14] T. van Leent, M. Bock, F. Fertig, R. Garthoff, S. Eppelt, Y. Zhou, P. Malik, M. Seubert, T. Bauer, W. Rosenfeld, W. Zhang, C. Becher, and H. Weinfurter, Entangling single atoms over 33 km telecom fibre, *Nature* **607**, 69 (2022).
- [15] M. Bock, P. Eich, S. Kucera, M. Kreis, A. Lenhard, C. Becher, and J. Eschner, High-fidelity entanglement between a trapped ion and a telecom photon via quantum frequency conversion, *Nat. Commun.* **9**, 1998 (2018).
- [16] T. Walker, K. Miyanishi, R. Ikuta, H. Takahashi, S. Vartabi Kashanian, Y. Tsujimoto, K. Hayasaka, T. Yamamoto, N. Imoto, and M. Keller, Long-distance single photon transmission from a trapped ion via quantum frequency conversion, *Phys. Rev. Lett.* **120**, 203601 (2018).
- [17] V. Krutyanskiy, M. Meraner, J. Schupp, V. Krcmarsky, H. Hainzer, and B. P. Lanyon, Light-matter entanglement over 50 km of optical fibre, *Npj Quantum Inf.* **5**, 72 (2019).
- [18] T. van Leent, M. Bock, R. Garthoff, K. Redeker, W. Zhang, T. Bauer, W. Rosenfeld, C. Becher, and H. Weinfurter, Long-distance distribution of atom-photon entanglement at telecom wavelength, *Phys. Rev. Lett.* **124**, 010510 (2020).
- [19] S. Langenfeld, P. Thomas, O. Morin, and G. Rempe, Quantum repeater node demonstrating unconditionally secure key distribution, *Phys. Rev. Lett.* **126**, 230506 (2021).
- [20] N. Kalb, A. A. Reiserer, P. C. Humphreys, J. J. W. Bakermans, S. J. Kamerling, N. H. Nickerson, S. C. Benjamin, D. J. Twitchen, M. Markham, and R. Hanson, Entanglement distillation between solid-state quantum network nodes, *Science* **356**, 928 (2017).
- [21] I. V. Inlek, C. Crocker, M. Lichtman, K. Sosnova, and C. Monroe, Multispecies trapped-ion node for quantum networking, *Phys. Rev. Lett.* **118**, 250502 (2017).
- [22] D. Hucul, I. V. Inlek, G. Vittorini, C. Crocker, S. Debnath, S. M. Clark, and C. Monroe, Modular entanglement of atomic qubits using photons and phonons, *Nat. Phys.* **11**, 37 (2014).
- [23] V. Krutyanskiy, M. Canteri, M. Meraner, J. Bate, V. Krcmarsky, J. Schupp, N. Sangouard, and B. P. Lanyon, Telecom-wavelength quantum repeater node based on a trapped-ion processor, *Phys. Rev. Lett.* **130**, 213601 (2023).
- [24] P. Drmota, D. Main, D. P. Nadlinger, B. C. Nichol, M. A. Weber, E. M. Ainley, A. Agrawal, R. Srinivas, G. Araneda, C. J. Ballance, and D. M. Lucas, Robust quantum memory in a trapped-ion quantum network node, arXiv Preprint ArXiv:2210.11447 (2022).
- [25] C. Simon, H. de Riedmatten, M. Afzelius, N. Sangouard, H. Zbinden, and N. Gisin, Quantum repeaters with photon pair sources and multimode memories, *Phys. Rev. Lett.* **98**, 190503 (2007).
- [26] O. A. Collins, S. D. Jenkins, A. Kuzmich, and T. A. B. Kennedy, Multiplexed memory-insensitive quantum repeaters, *Phys. Rev. Lett.* **98**, 060502 (2007).
- [27] M. Afzelius, C. Simon, H. de Riedmatten, and N. Gisin, Multimode quantum memory based on atomic frequency combs, *Phys. Rev. A* **79**, 052329 (2009).
- [28] N. Sinclair, E. Saglamyurek, H. Mallahzadeh, J. A. Slater, M. George, R. Ricken, M. P. Hedges, D. Oblak, C. Simon, W. Sohler, and W. Tittel, Spectral multiplexing for scalable quantum photonics using an atomic frequency comb quantum memory and feed-forward control, *Phys. Rev. Lett.* **113**, 053603 (2014).
- [29] A. Seri, D. Lago-Rivera, A. Lenhard, G. Corrielli, R. Oselimane, M. Mazzera, and H. de Riedmatten, Quantum storage of frequency-multiplexed heralded single photons, *Phys. Rev. Lett.* **123**, 080502 (2019).
- [30] T.-S. Yang, Z.-Q. Zhou, Y.-L. Hua, X. Liu, Z.-F. Li, P.-Y. Li, Y. Ma, C. Liu, P.-J. Liang, X. Li, Y.-X. Xiao, J. Hu, C.-F. Li, and G.-C. Guo, Multiplexed storage and real-time manipulation based on a multiple degree-of-freedom quantum memory, *Nat. Commun.* **9**, 3407 (2018).
- [31] D. Lago-Rivera, S. Grandi, J. V. Rakonjac, A. Seri, and H. de Riedmatten, Telecom-heralded entanglement between multimode solid-state quantum memories, *Nature* **594**, 37 (2021).
- [32] D. Lago-Rivera, J. V. Rakonjac, S. Grandi, and H. d. Riedmatten, Long distance multiplexed quantum teleportation from a telecom photon to a solid-state qubit, *Nat. Commun.* **14**, 1889 (2023).
- [33] J. Schupp, V. Krcmarsky, V. Krutyanskiy, M. Meraner, T. Northup, and B. Lanyon, Interface between trapped-ion qubits and traveling photons with close-to-optimal efficiency, *PRX Quantum* **2**, 020331 (2021).
- [34] J. Schupp, Ph.D. thesis, Interface between trapped-ion qubits and travelling photon with close-to-optimal efficiency, University of Innsbruck, 2021.
- [35] V. Krutyanskiy, M. Meraner, J. Schupp, and B. P. Lanyon, Polarisation-preserving photon frequency conversion from a trapped-ion-compatible wavelength to the telecom C-band, *Appl. Phys. B* **123**, 228 (2017).
- [36] A. Stute, B. Casabone, P. Schindler, T. Monz, P. O. Schmidt, B. Brandstätter, T. E. Northup, and R. Blatt, Tunable ion-photon entanglement in an optical cavity, *Nature* **485**, 482 (2012).
- [37] E. Bersin *et al.*, Development of a Boston-area 50-km fiber quantum network testbed, *Phys. Rev. Appl.* **21**, 014024 (2024).
- [38] A. Treiber, A. Poppe, M. Hentschel, D. Ferrini, T. Lorünser, E. Querasser, T. Matyus, H. Hübel, and A. Zeilinger, A fully automated entanglement-based quantum cryptography system for telecom fiber networks, *New J. Phys.* **11**, 045013 (2009).
- [39] S. A. Hill and W. K. Wootters, Entanglement of a pair of quantum bits, *Phys. Rev. Lett.* **78**, 5022 (1997).

- [40] P. Kobel, M. Breyer, and M. Köhl, Deterministic spin-photon entanglement from a trapped ion in a fiber Fabry-Perot cavity, *npj Quantum Inf.* **7**, 6 (2021).
- [41] M. Teller, V. Messerer, K. Schüppert, Y. Zou, D. A. Fioretto, M. Galli, P. C. Holz, J. Reichel, and T. E. Northup, Integrating a fiber cavity into a wheel trap for strong ion-cavity coupling, *AVS Quantum Sci.* **5** (2023).
- [42] C. Christoforou, C. Pignot, E. Kassa, H. Takahashi, and M. Keller, Enhanced ion-cavity coupling through cavity cooling in the strong coupling regime, *Sci. Rep.* **10**, 15693 (2020).
- [43] V. Krutyanskiy, M. Canteri, M. Meraner, V. Krcmarsky, and B. Lanyon, Multimode ion-photon entanglement over 101 kilometers [Data set], In PRX Quantum, Zenodo (2024), <https://doi.org/10.5281/zenodo.10864454>.
- [44] Y. Zhou, P. Malik, F. Fertig, M. Bock, T. Bauer, T. van Leent, W. Zhang, C. Becher, and H. Weinfurter, Long-lived quantum memory enabling atom-photon entanglement over 101 km of telecom fiber, *PRX Quantum* **5**, 020307 (2024).
- [45] S. Begley, M. Vogt, G. K. Gulati, H. Takahashi, and M. Keller, Optimized multi-ion cavity coupling, *Phys. Rev. Lett.* **116**, 223001 (2016).